energies

MDPI

Article

Spatial Graphene Structures with Potential for Hydrogen Storage

Krzysztof Jastrzębski *, Marian Cłapa, Łukasz Kaczmarek, Witold Kaczorowski, Anna Sobczyk-Guzenda, Hieronim Szymanowski, Piotr Zawadzki and Piotr Kula

Institute of Materials Science and Engineering, Lodz University of Technology, Stefanowskiego 1/15, 90-924 Lodz, Poland; lukasz.kaczmarek@p.lodz.pl (Ł.K.); witold.kaczorowski@p.lodz.pl (W.K.); anna.sobczyk-guzenda@p.lodz.pl (A.S.-G.); hieronim.szymanowski@p.lodz.pl (H.S.); piotr.zawadzki@p.lodz.pl (P.Z.); piotr.kula@p.lodz.pl (P.K.)

* Correspondence: krzysztof.jastrzebski@p.lodz.pl

Abstract: Spatial graphene is a 3D structure of a 2D material that preserves its main features. Its production can be originated from the water solution of graphene oxide (GO). The main steps of the method include the crosslinking of flakes of graphene via treatment with hydrazine, followed by the reduction of the pillared graphene oxide (pGO) with hydrogen overpressure at 700 °C, and further decoration with catalytic metal (palladium). Experimental research achieved the formation of reduced pillared graphene oxide (r:pGO), a porous material with a surface area equal to 340 m^2/g. The transition from pGO to r:pGO was associated with a 10-fold increase in pore volume and the further reduction of remaining oxides after the action of hydrazine. The open porosity of this material seems ideal for potential applications in the energy industry (for hydrogen storage, in batteries, or in electrochemical and catalytic processes). The hydrogen sorption potential of the spatial graphene-based material decorated with 6 wt.% of palladium reached 0.36 wt.%, over 10 times more than that of pure metal. The potential of this material for industrial use requires further refining of the elaborated procedure, especially concerning the parameters of substrate materials.

Keywords: 3D graphene; spatial structures; hydrazine pillars; manufacturing technology; hydrogen sorption

Citation: Jastrzębski, K.; Cłapa, M.; Kaczmarek, Ł.; Kaczorowski, W.; Sobczyk-Guzenda, A.; Szymanowski, H.; Zawadzki, P.; Kula, P. Spatial Graphene Structures with Potential for Hydrogen Storage. *Energies* **2024**, *17*, 2240. https://doi.org/10.3390/en17102240

Academic Editor: K. T. Chau

Received: 29 March 2024
Revised: 24 April 2024
Accepted: 27 April 2024
Published: 7 May 2024

1. Introduction

According to the "Global Hydrogen Review 2023" developed by the International Energy Agency (IEA), the demand for hydrogen in 2022 accounted for 2.5% of global energy consumption (over 95 million tons). According to forecasts for 2030. that amount will rise by at least 25% [1]. Hydrogen and its storage play a vital role in the widespread adoption in various sectors of green approaches, contributing to global sustainable and pro-ecological efforts. On the one hand, hydrogen is seen as a promising fuel for zero-emission vehicles—particularly fuel cell electric vehicles but also combustion engines [2–6]. It can also help to balance the electricity grid and may even be fundamental for new micro grids because its production may be related to storing excess renewable energy generated from variable sources. This means that it has potential as fuel, as a way of enhancing energy security and electrical grid stability, and as a pro-ecological compound. Regardless of its potential, the applicability of hydrogen is inevitably related to its methods of storage including compression, liquefaction, adsorption, absorption, and chemical storage. Solid-state storage methods, such as metal hydrides or recently developed carbon-based materials, present many advantages. Such systems are safer than equivalents for gaseous or liquid hydrogen because they are inherently stable and less prone to leakage or explosion risks. Moreover, they are easier to handle and transport, simplifying logistics and infrastructure requirements since the process of gas sorption/desorption may be easily controlled by changing the bed temperature. Among the obstacles to overcome on the way to their global popularization are their low sorption potential (correlating with the high overall mass of

storage systems) and the adjustment of process parameters (like temperature and pressure) to as close as possible to normal conditions.

Hydrogen storage is very attractive, but there are many formidable challenges in terms of practical capacity and kinetics. Whether it is the chemisorption of dissociated atomic hydrogen or the physisorption of molecular hydrogen, it is highly dependent on the surface interaction characteristic of different materials. High-surface-area, carbon-based materials and metal hydrides are the two most likely groups of materials cited in many reports. With the first article on hydrogen spillover and storage in carbon nanotubes by Dillon et al. [7], carbon-based materials became a real alternative to metal oxides for using hydrogen spillover for storage. However, carbon atoms do not participate directly in the reaction as a catalyst because of their higher inertness relative to conventional oxide supports.

Carbon-based materials such as fullerenes, nanotubes, and graphene and its spatial structure show great potential for being a hydrogen sorbing bed, which was confirmed by molecular modeling. Sorption at the level of 6–9 wt.% (or even higher) was unfortunately achieved only for computational models or was connected to highly troublesome aspects (like partial decomposition during hydrogen release [8], leading to hydrogen contamination with volatile hydrocarbons [9] in the case of fullerenes). Research has focused on the possibility of using the spillover phenomenon, especially with a palladium or platinum catalyst [10–12] and spatial graphene based on a crosslinking structure or by incorporating particles [13–16].

Spatial graphene can be classified according to pore size, as recommended by the International Union of Pure and Applied Chemistry (IUPAC): microporous graphene (pores smaller than 2 nm), mesoporous (2–50 nm), and macroporous (larger than 50 nm) [17]. The pore size distribution results from the manufacturing method of the spatial structure as well as from modifications of the graphene itself. In research on graphene aerogel (with pores in the range of 3–5 nm), Xu et al. and Han et al. showed that doping with nitrogen resulted in obtaining micropores and, in the case of phosphorus addition, mesopores [18,19]. Mesoporous graphene structures were also obtained through the introduction of long-chain polyamide for the sake of separation of the graphene planes [20]. Among chemical compounds that can act as pillars leading to three-dimensional structures are also polyethyleneimine [21], poly(vinyl alcohol) [22], and hydrazine [23]. Pillared nanostructures are also achieved by combining carbon nanotubes (CNT) and graphene [24]. Research in this field is conducted in particular to improve the mechanical properties of obtained materials. Moradi et al. [25], working with defective graphene, showed a reduction in stress concentration by the introduction of a CNT–graphene junction supporting existing holes. A honeycomb-like molecular structure of graphene obtained with the use of CNT and known as a pillared graphene block exhibited good mechanical properties in tensile tests [26]. Challenges to the development and industrial scaling of spatial graphene materials include raising the gravimetric density of hydrogen storage to at least 6.5 wt.%. This can be achieved by, for example, significantly increasing the open surface area of beds. Another aspect is the standardization of raw materials for maximum chemical purity. In the case of materials based on graphene oxide (GO) or its reduced form (RGO), this may be also related to a high degree of flake exfoliation (with monolayer dominance). Materials benefiting from the spillover phenomenon require not only the adjustment of the spillover catalysts themselves but also their size, distribution, way of integrating with the bed, etc. The main purpose of this paper is to present a method for the production and characterization of nitrogen-pillared spatial porous graphene with a high specific surface area. Through the further decoration of the material with a metal catalyst (palladium), the possibility of preparing a potential bed for hydrogen sorption is shown.

2. Materials and Methods

2.1. Manufacturing of a Spatial Graphene Bed

The process of manufacturing a hydrogen-absorbing bed requires a series of technological stages:

1. Cross-linking GO below 55 °C with hydrazine and pillared graphene oxide (pGO);

2. Material shredding;
3. Drying pGO at 60 °C;
4. Reducing and purifying pGO with hydrogen overpressure to obtain reduced pillared graphene oxide (r:pGO);
5. Decorating r:pGO with palladium;
6. Finally drying the spatial graphene-based bed at 60 °C.

2.1.1. Crosslinking GO and Its Further Purification

The formation of pGO was conducted with the use of hydrazine but in temperatures not exceeding 55 °C. In such mild conditions, the reagent did not fully behave as a reducing agent, but could be attached to the graphene surface. The result was the incorporation of the N-N segment between the flakes acting as the pillar of newly created, non-flat material.

The proposed use of hydrazine not as a reducing agent (which occurs at a temperature of about 100 °C) but as a compound that cross-links the graphene oxide suspension is a key point of the formation of pGO. This concept was confirmed experimentally on a model material—a monolayer, quasi-monocrystalline metallurgical graphene called high-strength metallurgical graphene (HSMG) [27]. The formation of the spatial graphene bed was started in line with the protocol presented in Section 2.1. The source of carbon was a water-based suspension of graphene oxide (Advanced Graphene Products, Zielona Góra, Poland) at a concentration of 10 wt.% Before the exact procedure, the solution was sonicated for 30 min in an open vessel to ensure its proper dispersion. Next, with sonication still present, the excess of hydrazine (Sigma-Aldrich, Stainheim, Germany) was slowly added to the system over a period of 10 s (ratio of hydrazine to graphene equal to 10:1). After 180 s, the temperature of the system underwent a periodical change in the range of 25 and 55 °C over the next 48 h. After that time, the water phase was separated from the graphene one. After removing the water, the synthesized product was preliminarily ground (in order to obtain domains no longer than 4 mm), air-dried for around 24 h, and, in the end, dried in an oven for 5 to 10 h at 60 °C.

After the drying process, the cross-linked graphene structure was further reduced (to eliminate the residual oxygen groups unsubstituted with hydrazine) using gaseous hydrogen. The process of annealing (hydrogen reduction) of the cross-linked structure was carried out in a tubular vacuum furnace. The experimental aperture was built with the use of the following main subsystems: furnace (Industrial Institute of Electronics, Warsaw, Poland), control unit, and vacuum block (Unitra, Warsaw, Poland). Portions of pGO were heated to 700 °C for 20 min in a hydrogen flow of 75 sccm and overpressure of about 400 Pa. In the consecutive stage, pGO was annealed for a further 180 min. Next, the material was cooled in a furnace to a temperature of 500 °C to start the evacuation of the process chamber to a pressure of about 10^{-3} Pa. Airing of the experimental apparatus and sample removal finalized the process after about 12 h, leading to r:pGO.

2.1.2. Decorating the Graphene-Based Bed with Palladium

According to the spillover phenomenon, metal catalysts such as palladium (but also platinum or nickel) take part in the dissociative chemisorption of hydrogen that is further migrating (already in the atomic form) onto the surface of the support [10–12]. The incorporation of the palladium catalyst into the graphene-based bed was performed by a wet procedure involving acidic baths. The initial reaction mixture was composed of $PdCl_2$ (VWR, Gdańsk, Poland), distilled water, and HCl added in the amount required to obtain a pH of the solution equal to 1. Such conditions allowed us to obtain the ionic complex of tetrachloropalladate $[PdCl_4]^{2-}$, which is highly soluble in water, and the entire solution became a transparent brown color. After soaking the r:pGO granules in this mixture and 60 min of intensive stirring, the solution was cooled to 7–12 °C and an aqueous solution of $NaBH_4$ (Sigma-Aldrich, Stainheim, Germany) at the same temperature was added (slowly dropwise). The reaction was visualized by the discoloration of the solution and the formation of a dark precipitate. The solution was then heated at 90 °C for 2 h with constant

stirring. After sedimentation of the decorated r:pGO, decantation was performed. r:pGO was washed several times with distilled water to remove unreacted substances and finally filtered using filter paper. The decorated spatial graphene-based deposit was ready for use after air-drying at 60 °C for another 12 h. The ratio of reagents and r:pGO was adjusted to obtain a 6 wt.% decorated bed and catalyst. To compare the results of the sorption potential, an undecorated bed (r:pGO) and a pure catalyst (platinum) were prepared in the same way.

2.2. Assessment of the Physicochemical Properties

The overall assessment of pGO and r:pGO involved the evaluation of morphology, specific surface area, chemical structure, and basic electrical properties to prove the successful manufacturing of a spatial graphene-based bed. The process of decoration did not involve the chemical interaction of the r:pGO or any of the used chemicals, so no significant changes in the abovementioned parameters were assumed.

2.2.1. Fourier-Transform Infrared Spectroscopy (FTIR)

Infrared absorption of the graphene samples in the spectral range of 4000 to 400 cm^{-1} was measured with a Fourier transform infrared spectrometer model iS50 (Thermo Fisher Scientific Inc., Waltham, MA, USA). Spectra were recorded with a resolution of 2 cm^{-1} using a high-sensitivity MCT-B detector-Mercury Cadmium Telluride (Thermo Fisher Scientific Inc., Waltham, MA, USA). The measurements were performed in a reflection mode with the application of a Sequelle DRIFT accessory working at an angle of incidence equal to 15 degrees. In each case, data from 256 scans were collected.

2.2.2. Evaluation of Specific Surface Area

The evaluation of specific surface area was performed for the samples after the 4th and 5th stages of the manufacturing process. For this purpose, the Sorpotomatic 1900 apparatus (Carlo Erba Instruments, Cornaredo, Italy) was used. The measurement was based on the low-temperature nitrogen adsorption mechanism. Before the measurement, the samples were annealed at 350 °C for 5 h in a 10^{-2} Pa vacuum in order to remove the adsorbed air particles (N_2, O_2, CO_2) and water vapor from the surface. The measurement was carried out at the temperature of liquid nitrogen (−196 °C) at relative pressure in the range of 0.04 to 1.

The specific surface area of examined samples was determined based on the Brunauer–Emmett–Teller (BET) theory. The calculations of the pore volume distribution function in the tested samples, depending on their diameters, were made according to the theory of Barret, Joyner, and Halenda (BJH). The calculations were made for the adsorptive branch of the isotherm for pores with a diameter greater than 0.7 nm.

The linear form of the BET equation was as follows:

$$\frac{1}{W\left(\frac{P}{P_o}\right)-1} = \frac{1}{C\,W_m} + \frac{C-1}{C\,W_m}\left(\frac{P}{P_0}\right) \quad (1)$$

where

P/P_0—relative pressure,
W—adsorbate mass,
C—constant depending on the difference between the heat of the adsorption for the first layer and the heat of the condensation of the adsorbate,
W_m—mass of the monolayer of the adsorbate.

After determining W_m from the above equation, it was possible to determine the specific surface area SBET, based on the following equation:

$$S_{BET} = \frac{W_m N A_{GS}}{M}\frac{1}{W\left(\frac{P}{P_o}\right)-1} = \frac{1}{C\,W_m} + \frac{C-1}{C\,W_m}\left(\frac{P}{P_0}\right) \quad (2)$$

where

S_{BET}—specific surface area,
N—Avogadro's number,
A_{GS}—the surface area occupied by one adsorbate molecule in a monolayer, i.e., the sitting area (for nitrogen, A_{GS} = 0.162 nm was assumed).

2.2.3. Raman Spectroscopy

The InVia Raman spectrometer (Renishaw, Sheffield, UK) was used in this research. All experiments were performed with a 532 nm laser and a ×50 lens. Spectra in the Raman shift ranging from 1100 cm^{-1} to 3200 cm^{-1} were analyzed at a spectral resolution of 1 cm^{-1}. Raman scattering time of 30 s and laser power on the sample of 0.5 mW were maintained. The spectrum obtained in this way was deconvolved using the PEAKFIT 4.12 program. The band in the range of 1100 to 1800 cm^{-1} was defined by 3 characteristic peaks: D, G, and D′, while the band from 2500 to 3200 cm^{-1} was defined by 4 peaks: D + D″, D*, 2D, and D + D′ [27–30].

2.2.4. Electrical Measurements

The resistance of the spatial graphene after the reaction with hydrazine and after heating with hydrogen overpressure was measured using the authors' equipment: a non-conductive tube with an internal diameter of d = 8.7 mm equipped with two aluminum electrodes at the ends—one fixed and one movable (see Figure 1). Initially, the tested spatial graphene loosely filled the tube bulk height (0). Then, with the help of a moving electrode, the test sample was compressed, measuring its height and electrical resistance. The measurement was conducted till the value of the force of compression was equal to 50 N. Based on the collected data, the resistivity (specific resistance) was determined, expressed in the Ω*cm unit. The compressibility and density of the measured material were also assessed.

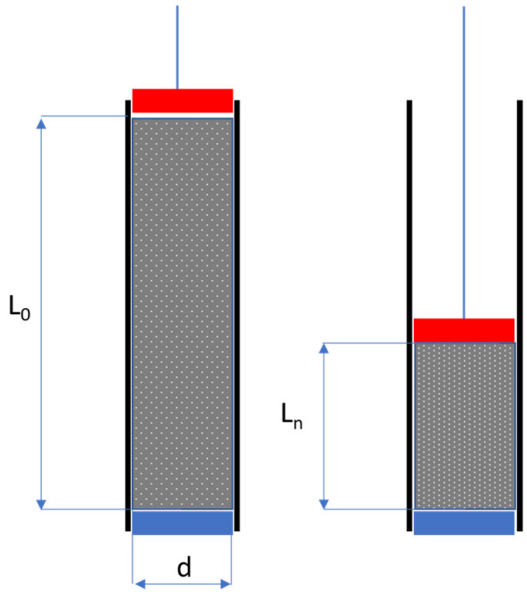

Figure 1. The idea for measuring the resistivity of pGO and r:pGO (d—tube inner diameter; L_0—the bulk height; L_n—the height of the compressed spatial graphene at the nth measurement).

2.3. Assessment of the Potential for Hydrogen Storage

The processes of sorption/desorption of hydrogen were performed on three types of sample: pure catalyst prepared in a way resembling the decoration of the bed but without the spatial graphene-based material; r:pGO; and palladium-decorated r:pGO (concentration of catalyst equal to 6 wt.%). The time between the manufacturing of each sample and the conditions of their storage were kept similar.

The procedure for the evaluation of the sorption/desorption potential of the tested samples was carried out using the experimental system shown in Figure 2. It consisted of a measuring chamber (with a capacity of 13 mL) made of quartz glass, a vacuum pump, a hydrogen dosing system, and temperature and pressure measurement sensors. The absorbing material was placed in the part of the chamber with the larger diameter. This part of the measuring chamber was introduced into the furnace during the measurement and heated to the set temperature. The control and data acquisition system recorded temperature and pressure changes.

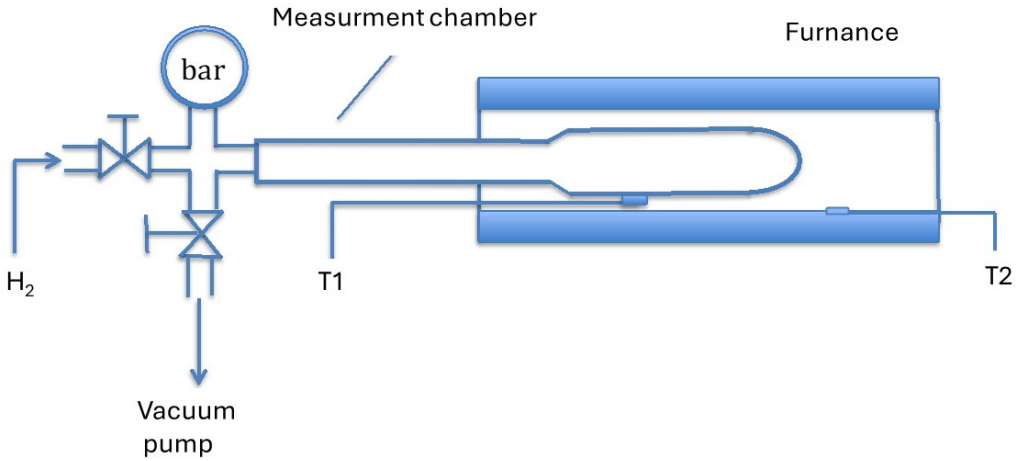

Figure 2. Scheme of the equipment used to determine the sorption potential of hydrogen.

The assessment procedure of sorption/desorption involved cyclic heating and cooling of the measuring chamber filled with the sorbing bed. The recorded data allowed us to determine the pressure differences between points with different temperatures and, consequently, calculate the amount of gas absorbed. Calculations were carried out based on the Clapeyron–Mendeleev equation, assuming an isochoric transition of the gas remaining in the chamber and the gas sorption occurring in the tested material. It was assumed that the chamber consisted of two zones, hot and cold, with a symmetrical temperature gradient at the zone border and the same pressure inside the whole measuring chamber (total volume). The amount of gas absorbed was then equal to the difference between the amount of gas in the chamber at a temperature higher than the desorption temperature and its amount at a temperature lower than the absorption temperature and was determined using the following equation:

$$n = \left(\frac{p_B xV}{RT_A} + \frac{p_B(1-x)V}{RT_B}\right) - \left(\frac{p_A V}{RT_A}\right) \quad (3)$$

where

n—the number of moles of the gas absorbed,
p_A—absorption pressure,
p_B—desorption pressure,
T_A—absorption temperature,
T_B_desorption temperature,
xV—the volume of the quartz chamber "cold zone",
(1 − x)V—the volume of the quartz chamber "hot zone",
R—the universal gas constant.

The measurements were preceded by the activation process performed for 60 min at a temperature of 350 °C in the same chamber. During this process, the working atmosphere was exchanged several (3–10) times with the help of the vacuum pump and gaseous hydrogen of 99.999% purity. Sorption/desorption was achieved by the cyclic change of the

temperature of the hot zone (in the range of about 25–250 °C) by inserting the measurement chamber into the furnace or removing it.

3. Results and Discussion

3.1. FTIR

Figure 3 shows the spectra of GO (A), pGO (B), and r:pGO (C) obtained via hydrogen reduction in a furnace at 700 °C. In the spectrum presented in Figure 3A, the presence of the characteristic peak for GO was confirmed at a wavenumber of 1738 cm^{-1}. It was related to the stretching vibrations of C=O bonds of the carboxyl (COOH) and/or carbonyl (C=O) group. This functional group could attach to the graphene structure both along the edge of the flake and to its base plane. The presence of the carboxyl group was also confirmed by the presence of a peak with a maximum of 3400 cm^{-1} originating from the stretching vibrations of the O-H bonds. This band was wide, proving that a large number of hydroxyl groups were derived from water (constituting a medium reaction), linked together by intermolecular hydrogen bonds. Another characteristic region for GO was at 1200 cm^{-1}—the location of a peak resulting from the asymmetric vibrations of the C-OH stretching bonds, and at 1042 cm^{-1}, arising from vibrations of the C-O stretching bonds in the C-O-C system. At 1613 cm^{-1}, in all analyzed spectra, there was a peak related to the stretching vibrations of C=C bonds occurring in the hexagonal graphene rings. The bands linked with this structure occurred at 985 cm^{-1} and 585 cm^{-1}. In the wavelength range of 3000 to 2800 cm^{-1}, there were bands derived from stretching vibrations of both symmetrical and asymmetrical C-H bonds in aliphatic hydrocarbon chains attached to the ring structure of graphene. Such groups indicated impurities of this material, most likely created during its synthesis. Additionally, both in the spectra of GO and pGO cross-linked with hydrazine, there were peaks indicating the presence of SO_3H. A peak from this type of bond could also be found at a wavenumber equal to 1145 cm^{-1}. These were both symmetrical and asymmetric stretching vibrations. Additionally, deformational vibrations of the S=O bond were confirmed by the peak located at 585 cm^{-1}. The presence of SO_3H groups on the surface of the tested GO and pGO was the result of the residues of sulfuric acid used for the manufacturing of GO by the Hummers method.

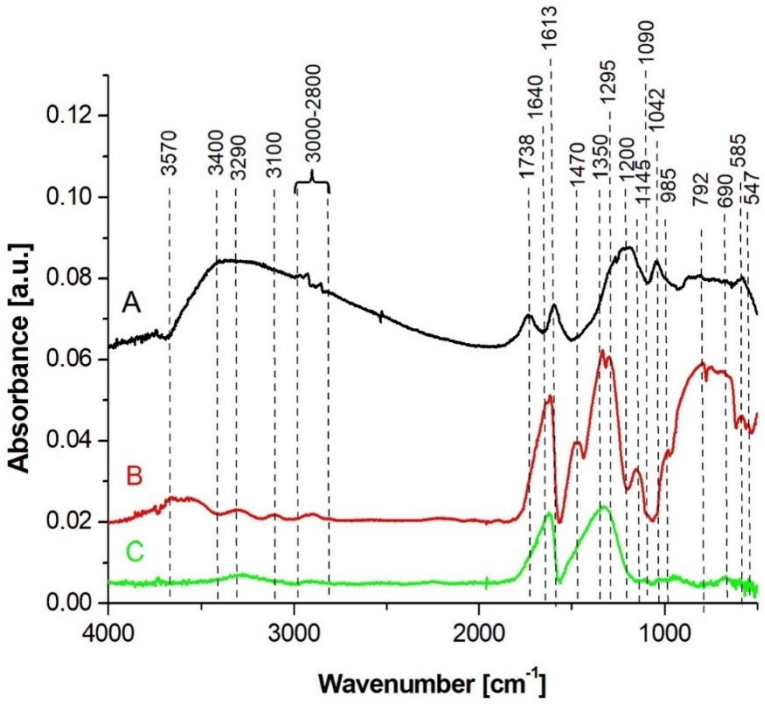

Figure 3. FTIR spectra obtained for graphene oxide (GO) (A), hydrazine-pillared graphene oxide (pGO) (B), and r:pGO hydrogenated in a furnace at 700 °C (C).

In the pGO spectrum, the peak at 1738 cm^{-1}, characteristic for GO, disappeared, and a new one appeared at 1640 cm^{-1}, which came from the C=O bonds occurring in amides. Reactions with hydrazine caused the appearance of new bonds derived from this reagent. One piece of evidence for this was a wide band with a maximum at 1470 cm^{-1}, belonging to the vibrations of the C-N bonds. The widened slope of this band in the wavenumber range 1480–1530 cm^{-1} confirmed the presence of N=N-O bonds in the structure of the material (asymmetric stretching vibrations). An additional peak from this type of bond was also found at 1350 cm^{-1} (symmetrical stretching vibrations). The presence of C-N bonds in the aromatic structure of the carbon chain was also visible at the wavenumbers of 1295 cm^{-1} and 792 cm^{-1}. Additionally, the presence of C-CN bonds was confirmed by the presence of the peak at 547 cm^{-1}. The pGO spectrum also revealed the appearance of vibrations of NH bonds at 3570 cm^{-1} (stretching vibrations), 3290 cm^{-1} (stretching vibrations as in amides), 3100 cm^{-1} (asymmetric stretching vibrations in NH_3^+), and 1090 cm^{-1} (vibrations extending toward the C-NH_2 moiety).

After annealing of the tested material with hydrogen overpressure, the cross-linked structure of the graphene was reduced. The majority of N-H and C-H bonds and all bonds characteristic of H_2SO_4 disappeared. The remaining peaks were characteristic of the hexagonal structure of graphene, and those remaining after modification with hydrazine at 1640 cm^{-1}, 1470 cm^{-1}, and 1295 cm^{-1} were still visible, but they were much less distinguished and had a lower intensity than before the reduction with hydrogen. This effect was visible in the case of both C-N and CON bonds.

3.2. BET

The results of the evaluation of specific surface area with the nitrogen adsorption method are presented in Figures 4 and 5. Figure 4 shows the sorption–desorption isotherms for pGO and r:pGO. According to the UPAC classification, the presented dependencies belong to type IV out of six existing ones [17]. Type IV applies to samples with well-developed micro and mesoporosities. In the tested powders, the presence of pores with a size of 2–50 nm was found. The specific surface area of the tested pGO powder was 130 ± 2 m^2/g. The same powder, subjected to reduction with hydrogen, had a specific surface area of 340 ± 2 m^2/g. Hydrogen reduction also caused a sharp (more than ten-fold) increase in the pore volume from 3.3 cm^3/g to 33.7 cm^3/g for the sample before and after hydrogen reduction, respectively.

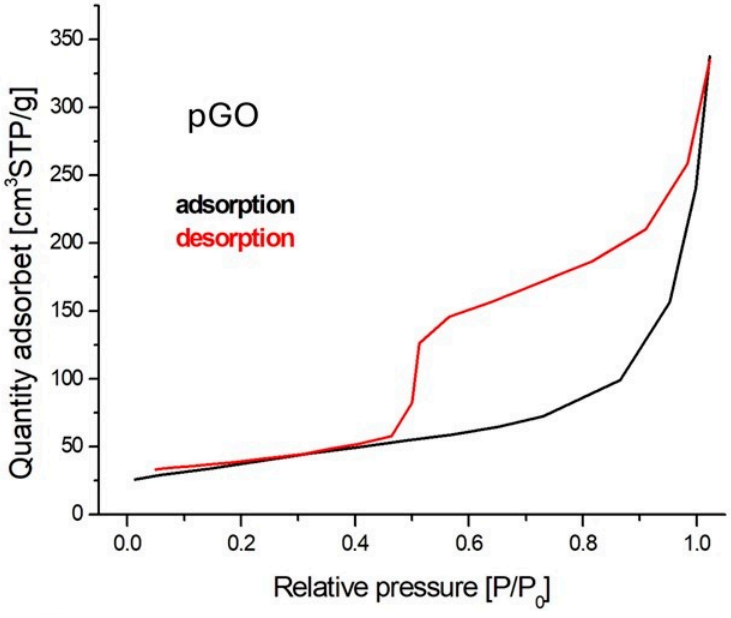

Figure 4. *Cont.*

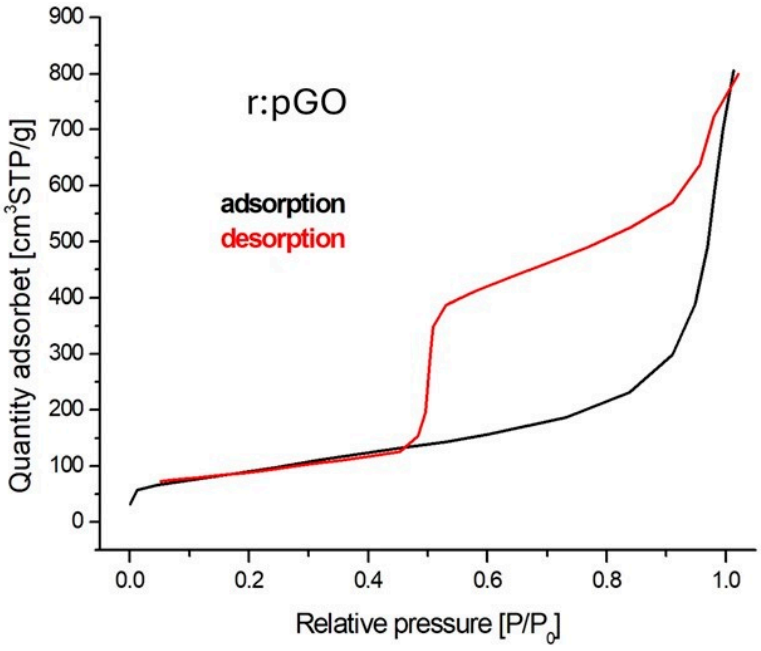

Figure 4. Nitrogen adsorption–desorption curve for pGO (**top**) and r:pGO (**bottom**), respectively.

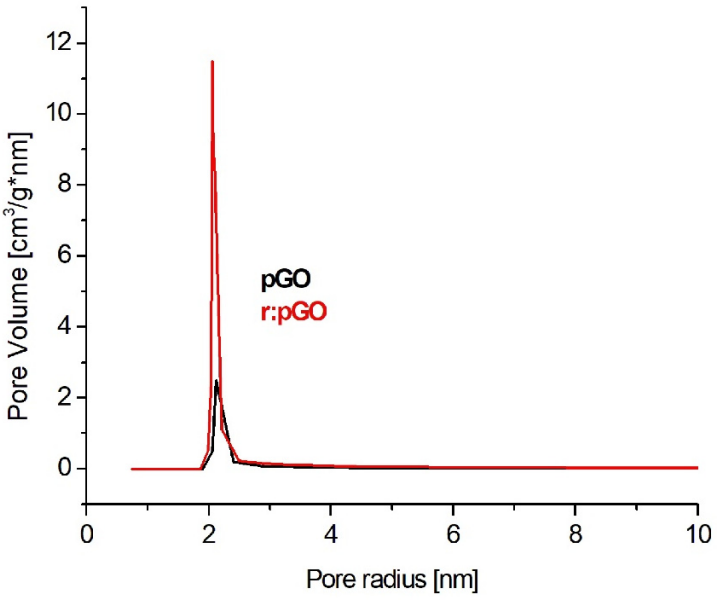

Figure 5. Pore size distribution in tested samples.

The theory of the physical adsorption of gases on micro- and mesoporous solids indicates that this process occurs through the formation of multilayers (layer by layer). For micro and mesoporous materials, the filling of pores takes place at relatively low relative pressures. The formation of an adsorption film on the mesoporous surface is followed by the final filling of the mesopore volume with a liquid adsorbate. This process is known as capillary condensation. The shape of the isotherm corresponds to the shape of the pores. A more detailed analysis of the obtained isotherm and the hysteresis shape indicated that the obtained isotherm belonged to type IV, and the hysteresis shape indicated subtype I-II. This arrangement was typical for bottle-type pores (narrow entrance to a large space) or pores formed between two flat planes. It could be assumed that the pores were the spaces between the graphene planes. The pore shape is shown in Figure 6.

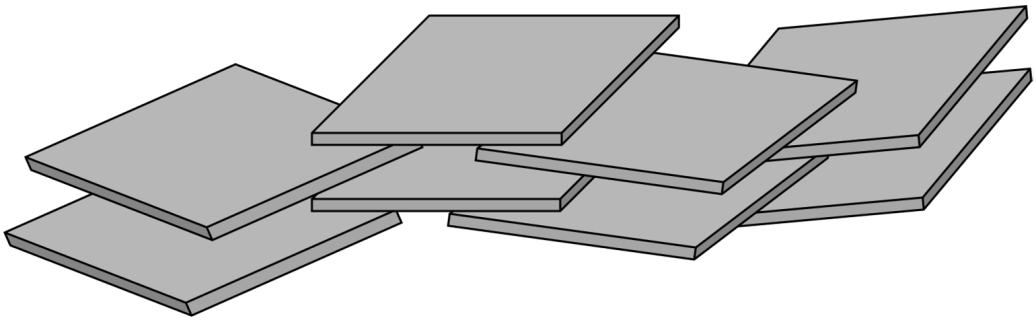

Figure 6. Scheme of the shape of pores in the tested samples.

Based on the results obtained from the measurements of nitrogen sorption and desorption, the dependence between pore diameter and volume was calculated using the BJH method. The calculation results for the graphene samples before and after reduction with hydrogen are shown in Figure 5.

The presented relationship shows that pores in the range of 1.9–2.3 nm dominated in both tested samples. This size represented 96% and 98% of the porosity present in the tested powders. It can be clearly stated that both tested materials were homogeneous in terms of pores distribution. It is worth noting that the size of the pores was completely in accordance with the size of the pillaring agent used. This proves the accuracy of the reagent used, which confirms the quality of the cross-linking (pillaring) method used for graphene oxide.

3.3. Raman Spectroscopy

Figure 7 presents the spectra of the graphene powders and the corresponding ID/IG ratios before and after hydrogen reduction, while Figure 8 shows the spectra after matching them with the main characteristic bands. Detailed data on the position and half width at half maximum (HWFM) of the examined peaks are presented in Table 1.

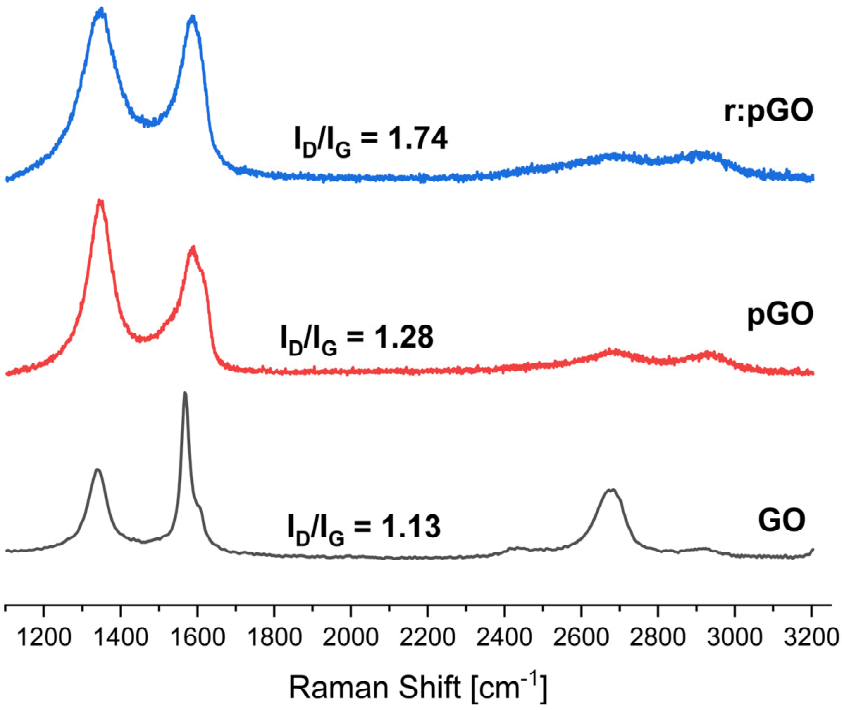

Figure 7. Raman spectra of GO, pGO, and r:pGO.

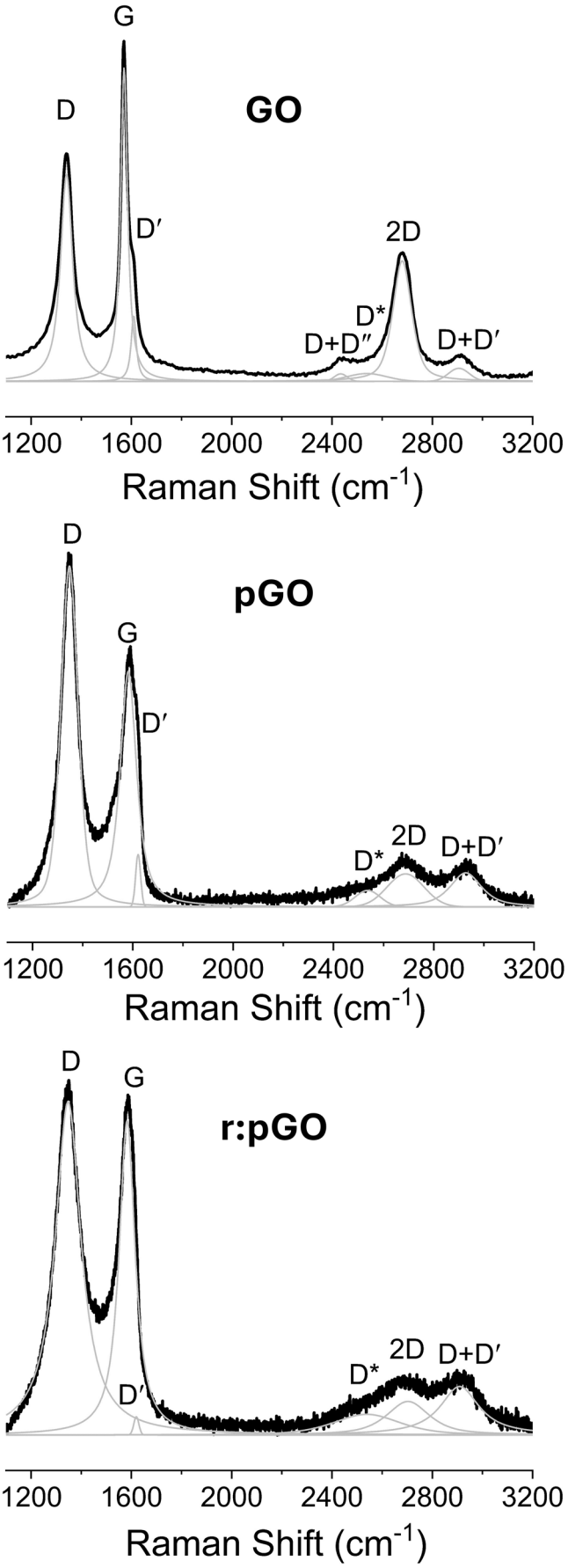

Figure 8. Fitting Raman spectra with characteristic bands: D, G, D′, D + D″, D*, 2D, D + D′.

Table 1. The values of the HFM and positions of the characteristic peaks for GO before and after modifications.

	D Band	G Band	D′ Band	D + D″ Band	D* Band	2D Band	D + D′ Band	I_{2D}/I_G
	FWHM/Position of the Band [cm^{-1}]							
GO	57.69/1341.34	33.04/1570.75	24.24/1609.03	60.05/2434.64	93.69/2538.84	88.38/2679.90	96.96/2905.67	0.87
pGO	80.03/1347.22	77.86/1582.11	23.42/1620.99	-	117.54/2536.62	172.97/2687.51	149.64/2927.74	0.68
r:pGO	124.49/1347.52	76.8/1583.06	23.99/1619.67	-	315.71/2538.98	202.28/2703.05	187.79/2909.01	0.25

Additionally, on the basis of the Tuinstra–Koenig model [28,31], the sizes of the crystallites in the sp2 (La) plane in the tested GO structures were calculated, which were 17 nm, 15 nm, and 13 nm for the GO, pGO, and r:pGO samples, respectively.

On the basis of the presented data, it was possible to distinguish most of the modes characterizing the graphene materials: D band (about 1350 cm^{-1}), G band (about 1580 cm^{-1}), D* band (about 2535 cm^{-1}), 2D band (about 2700 cm^{-1}), and D + D′ band (about 2900 cm^{-1}) [27,30,32,33]. The determined D′ bands (about 1620 cm^{-1}) proved that the structures were damaged [27]. Additionally, the Raman spectroscopy of GO contained the D + D″ peak, characteristic of ordered graphite structures [30], which could indicate the poor quality of this material.

The presented results of the Raman analysis showed the increasing number of defects in the modified powders, for which the ID/IG value increased from 1.13 to 1.28 after hydrazine cross-linking processes, and to 1.74 after hydrogenation of the cross-linking 3D structure. Similar conclusions were drawn by analyzing the shift in the value of the G peak before and after the modifications from about 1570 cm^{-1} to about 1582–1583 cm^{-1}. Such a shift, as stated by many researchers [34–36], can indicate the decreasing number of layers in graphene (for higher wavenumbers) in the case of pGO and r:pGO. For the GO sample, restacking appeared, which led to a graphitic-like structure. According to Gupta et al. [36], the number of graphene layers in manufactured spatial graphene is probably in the range of 1–5. This effect is widely described in the literature [27,33]. On the other hand, a continuous increase in the ID/IG ratio was evidence of the ongoing reduction processes in the GO powders, which was proven by FTIR analysis. In our case, no significant increase in ID/IG was observed between the GO powder and the material treated with hydrazine at 37 °C because, in this process, one of the probable reactions was the replacement of carboxyl groups with carbonyl groups. On the other hand, a large jump in the ID/IG ratio of the tested samples was visible after reduction with hydrogen overpressure. Therefore, it was expected that these would be the most damaged samples and that their structure would be the closest to that of rGO. In each of the analyzed cases, the intensities of the 2D peaks were lower than the intensities of the G peaks, and the constantly decreasing I2D/IG ratio was visible after each of the mentioned modifications. This could be proof of the decreasing number of graphene flakes building the structures or their better dispersion [27]. This decrease in the number of layers was also confirmed by the decreasing values of the crystallite sizes in the sp2 plane, calculated using the Tuinstra–Koenig model.

3.4. Electrical Measurements

The electrical resistance measurements made on the loosely packed graphene, both for pGO and r:pGO, were characterized by a wide range of values, oscillating in the range of several hundred ohms. The conductivity of spatial graphene has a percolating nature. It can be analyzed according to the model of fragmented conductive material (graphene) in an insulator (air). Then, the resistance depends on the density of the conductive material because the number of available conductive paths increases. In order to compare the conductive material itself for different samples, the influence of percolation conductivity had to be minimized. With the increase of the compressive force, similar resistance values were obtained for samples of a given type. Table 2 summarizes the results averaged after pressing with a force of 50 N, for three series of measurements, for both types of spatial

graphene. The resistivity value for r:pGO was about 12 times lower compared to the results obtained for pGO. This meant that cross-linked graphene oxide after treatment with hydrazine underwent reduction during annealing with hydrogen overpressure.

Table 2. Measurements of the resistivity of spatial graphene powder.

	After	Resistivity [Ωcm]	Density [g/cm^3]	Compressibility
pGO	hydrazine	15 ± 2	0.15 ± 0.05	approx. 50%
r:pGO	annealing	1.2 ± 0.3	0.09 ± 0.05	approx. 30%

3.5. Sorption/Desorption of Hydrogen

A graphical representation of the process parameters during the sorption/desorption of hydrogen by the examined samples (pure palladium, pure graphene bed—r:pGO, and graphene bed decorated with metal catalyst) is presented in Figures 9–11. The conducted calculations show that the pure spatial graphene-based bed did not absorb hydrogen within the assumed working range of 25–250 °C. The data for the pure catalyst are in line with claims in the literature for palladium. In the case of the experimental research, the achieved value was equal to 0.56 wt.%. By the addition of a catalyst to the carbon bed, the sorption of the material increased to 0.36 wt.%. Knowing that the amount of palladium was only 6% of the total mass of the bed, the absorption of only the catalyst should have been equal to about 0.034 wt.%. The obtained value of over 0.3 wt.% proves the phenomenon of spillover for the proposed material.

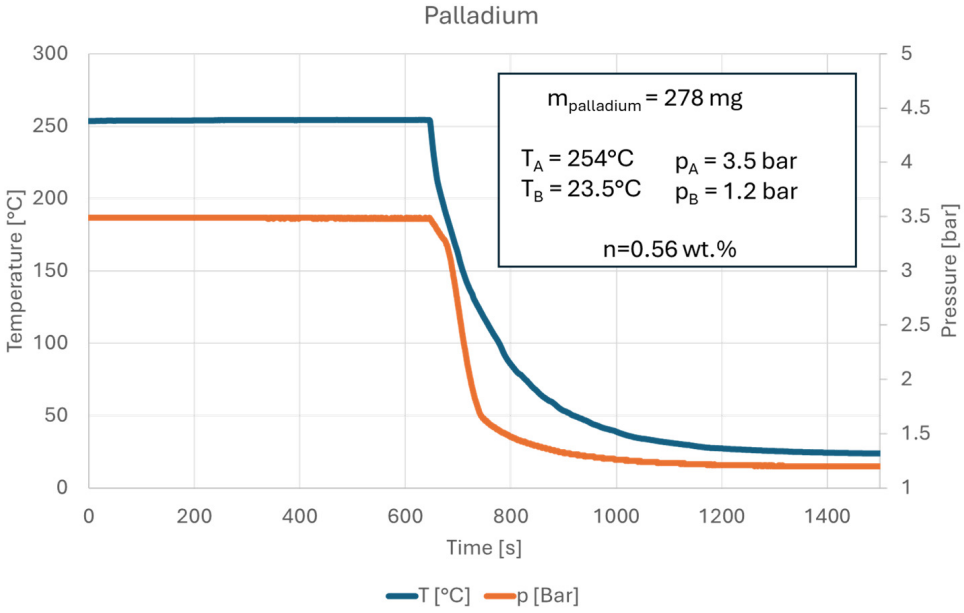

Figure 9. The course of hydrogen desorption for plain palladium.

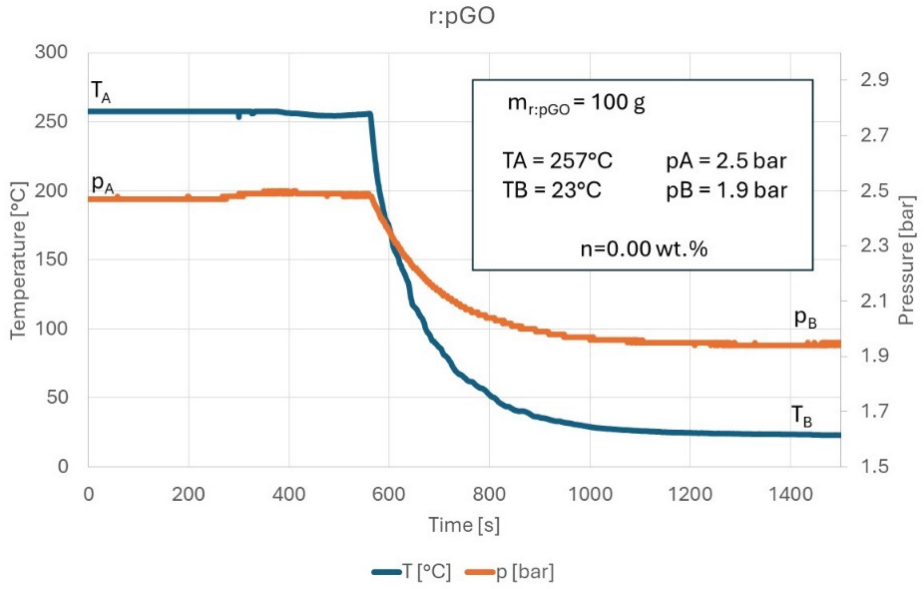

Figure 10. The course of the sorption process for the spatial graphene-based bed (r:pGO).

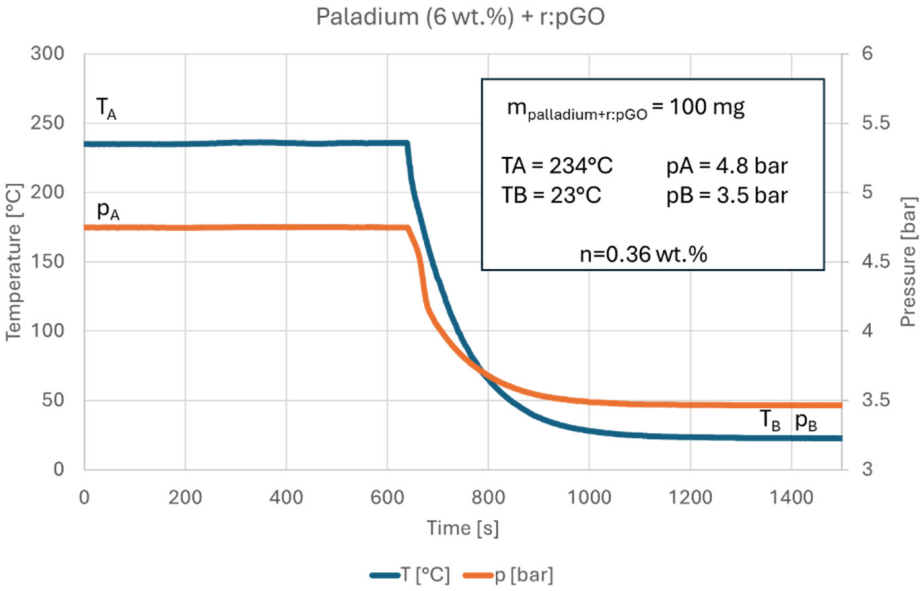

Figure 11. The course of the sorption process for the bed composed of spatial graphene decorated with 6 wt.% of palladium.

4. Summary

This publication presented a method of producing spatial r:pGO graphene as well as a wet method for its decoration with palladium to form a bed for hydrogen accumulation. A spatial structure with the quasi-2D properties of graphene became a reservoir intended for reversible hydrogen storage by eliminating $\pi - \pi$ interactions between the flakes. By separating them due to their pillaring, it was possible to relatively easily introduce hydrogen into the structure while maximizing its chemical bonding with the graphene carbon atoms. Not pillaring the graphene flakes would lead to reduced space between the flakes and the reconstruction of the graphite system. Thus, the ability to store hydrogen would be reduced. In graphite systems, the steric hindrance of potential C-H systems inside the structure effectively eliminates the possibility of chemical hydrogen bonding. Therefore, it is necessary to separate the individual graphene flakes from each other.

The explained manufacturing method can be easily adopted on an industrial scale. In the first stage, the addition of hydrazine to the GO suspension resulted in the formation of a -COON- or -CON- bond simultaneously with a mild reduction of GO. A characteristic effect was the precipitation of the spatial structures (pGO) from the reaction mixture as a result of cross-linking graphene flakes with pillars originating from hydrazine molecules. This structure resembled a para-graphitic structure, but the carbon planes located next to each other were situated within the distance determined by the size of the pillar-forming agent. Hydrazine decreased the number of groups attached to the surface of the flakes. This was proven by FTIR analysis, which showed a significant reduction in the intensity of the -OH and -COOH groups after the addition of the pillar-forming agent. This means that hydrazine has cross-linking properties; thus, it was possible to create spatial structures. The resulting porous material had a bulk density of 0.13 g/cm^3.

Heating the pGO at a high temperature in hydrogen led to a reduction of the remaining hydroxyl and carboxyl groups, which was confirmed by the increase in the electrical conductivity of the analyzed samples. The further rearrangement of the spatial structure was the direct effect of a rapid increase in the volume of water entrapped in the structure and its release during annealing with the overpressure of hydrogen. The loosening of the structure was indicated by direct observation of the increased volume of the sample after annealing. SEM analyses proved a change in the size of the observed grains, but BET indicated an increase in the specific surface area to 340 ± 2 m^2/g. This was also manifested by a decrease in the material's bulk density to 0.051 g/cm^3. Interestingly, during the hydrogen reduction process, the mass of the sample decreased. There was a 50% average difference in weight before and after the reduction. It is also interesting that the pillars forming the three-dimensional structure during cross-linking with hydrazine were resistant to the reduction with hydrogen, and remained in the majority of the material. This was indicated not only by FTIR analysis but also by BET. The pore size did not change after the hydrogen reduction process, but its number changed more than seven times. This may indicate that the process of hydrogen reduction and removing oxygen created new spaces, the size of which was determined by the nitrogen bridge. On the basis of the flake graphene, r:pGO was easily decorated by palladium using the wet method, forming a bed with the potential for vast application in the energy industry, e.g., for hydrogen storage, in batteries, or in electrochemical and catalytic processes.

The proposed spatial graphene-based bed decorated by palladium showed promising results concerning its potential for hydrogen storage in mild conditions (sorption/desorption temperature lower than 200 °C). This material achieved over ten times higher hydrogen sorption than the cumulative value for the separated constituents (palladium and spatial graphene). The low overall value of hydrogen sorption (only 0.39 wt.%) undoubtedly influenced the purity of the raw materials and caused insufficient surface development of the spatial graphene. It should be remembered that although a graphene sheet surface area of 2629 m^2/g seems theoretically accessible, the spatial forms of graphene are facing their limit. The common level of this parameter for such materials is now within the range of 700 m^2/g [37] up to about 1100 m^2/g [38], but recent declarations show even over 2000 m^2/g [39]. This means an improvement of this parameter by almost six times in comparison to values obtained for r:pGO previously described, which would be in line with the same improvement of hydrogen sorption. During the examination of the sorption/desorption processes, a layer of contaminants was deposited on the cold wall of the measuring chamber. It was determined that the white or white-pinkish precipitate was in fact composed of salts of manganese and residuals of acids used during the synthesis of GO from graphite using the Hummers method. The presence of residues from previous chemical treatments in the reacting bed may have negatively influenced the sorption potential of the material. The assessment of the number of impurities (present in the GO solution as well as residuals of further processes) suggested a possible improvement by a factor of at least 0.5. Based on this value, the reachable, reversible sorption of hydrogen would be over 3 wt.%, while further improvements may be achieved by adjusting the amount,

distribution, and type of catalysts. To sum up, the main advantages of the proposed bed are as follows: high specific surface area, which, by optimizing individual technological stages and reducing the contamination of raw materials, can be further improved by several times; open porosity and space available for gases or electrolytes throughout the entire volume of the material, not only on the external surface; and mild working temperature range.

5. Conclusions

Research is focusing on showing the potential for hydrogen storage of graphene-based beds. The proposed solution of a spatial carbon structure decorated with a platinum catalyst can be a novel method of energy storage that uses the spillover phenomenon The obtained results clearly show that the process of manufacturing the spatial graphene from graphene oxide is a two-step process. The conducted research achieved the formation of N-N bridges between the graphene flakes. Neither of the synthesis steps (crosslinking with hydrazine and high-temperature hydrogen reduction) led to the restacking of graphene, resulting in a predominantly graphitic or similar structure. We also obtained evidence of the ongoing spatial organization of reduced graphene oxide flakes and reduction processes.

The characterization of the physicochemical properties of the obtained three-dimensional graphene confirmed the possibility of the implementation of r:pGO manufacturing technology on a semi-industrial scale. By cross-linking GO with hydrazine followed by annealing with hydrogen overpressure, a conductive material based on flake graphene with a high specific surface area (about 340 ± 2 m^2/g) was obtained.

Sorption/desorption phenomena on the palladium-decorated spatial graphene-based bed prove the potential of this material for the reversible sorption/desorption of hydrogen; yet, the final sorption of hydrogen will be affected by further optimization of the bed material. In this way, spatial graphene-based beds are promising for storing this energy carrier.

6. Patents

This article is in accordance with patent no. PL244377B1 (Method of obtaining a micro/mesoporous conductive polymer with a spatial structure of graphene and high active surface) and patent application P. 442906 (Nano-, meso- or microstructured graphene composite for reversible hydrogen storage).

Author Contributions: Conceptualization, P.K.; methodology, M.C., Ł.K., H.S., P.K. and K.J.; validation, Ł.K. and H.S.; formal analysis, M.C. and Ł.K.; investigation, K.J., M.C., W.K., A.S.-G. and H.S.; resources, K.J. and P.Z.; data curation, M.C., W.K., A.S.-G. and H.S.; writing—original draft preparation, K.J., M.C., Ł.K., W.K., A.S.-G. and H.S.; writing—review and editing, K.J., M.C., H.S., P.Z. and P.K.; visualization, K.J. and H.S.; supervision, K.J. and P.K.; project administration, Ł.K., W.K. and P.K.; funding acquisition, W.K. and P.K. All authors have read and agreed to the published version of the manuscript.

Funding: This research was funded by The National Centre for Research and Development, grant number 4/H2/113/18/PU. This research was supported as part of the program co-financed by the European Regional Development Fund under sub 4.1.3 Innovative methods of research management of the Intelligent Development Operational Program 2014–2020, under the project entitled Raising the level of innovation in the economy by implementing a new model of financing groundbreaking research projects (no. POIR.04.01.03-00-0001/16).

Data Availability Statement: The data presented in this study are available upon request from the corresponding author.

Conflicts of Interest: The authors declare no conflicts of interest.

References

1. International Energy Agency. Global Hydrogen Review. 2023. Available online: www.iea.org (accessed on 12 March 2014).
2. Onorati, A.; Payri, R.; Vaglieco, B.M.; Agarwal, A.K.; Bae, C.; Bruneaux, G.; Canakci, M.; Gavaises, M.; Günthner, M.; Hasse, C.; et al. The role of hydrogen for future internal combustion engines. *Int. J. Engine Res.* **2022**, *23*, 529–540. [CrossRef]

3. Boretti, A. Hydrogen internal combustion engines to 2030. *Int. J. Hydrogen Energy* **2020**, *45*, 23692–23703. [CrossRef]
4. Algayyim, S.J.M.; Saleh, K.; Wandel, A.P.; Fattah, I.R.; Yusaf, T.; Alrazen, H.A. Influence of natural gas and hydrogen properties on internal combustion engine performance, combustion, and emissions: A review. *Fuel* **2024**, *362*, 130844. [CrossRef]
5. Falfari, S.; Cazzoli, G.; Mariani, V.; Bianchi, G.M. Hydrogen application as a fuel in internal combustion engines. *Energies* **2023**, *16*, 2545. [CrossRef]
6. Teoh, Y.H.; How, H.G.; Le, T.D.; Nguyen, H.T.; Loo, D.L.; Rashid, T.; Sher, F. A review on production and implementation of hydrogen as a green fuel in internal combustion engines. *Fuel* **2023**, *333 Pt 2*, 126525. [CrossRef]
7. Dillon, A.; Jones, K.; Bekkedahl, T.; Kiang, C.H.; Bethune, D.S.; Heben, M.J. Storage of hydrogen in single-walled carbon nanotubes. *Nature* **1977**, *386*, 377–379. [CrossRef]
8. Luzan, S.M.; Tsybin, Y.O.; Talyzin, A.V. Reaction of C60 with Hydrogen Gas: In Situ Monitoring and Pathways. *J. Phys. Chem. C* **2011**, *115*, 11484–11492. [CrossRef]
9. Talyzin, A.V.; Shulga, Y.M.; Jacob, A. Comparative study of hydrofullerides $C_{60}H_x$ synthesized by direct and catalytic hydrogenation. *Appl. Phys. A* **2004**, *78*, 1005–1010. [CrossRef]
10. Zhou, H.; Zhang, J.; Zhang, J.; Yan, X.; Shen, X.; Yuan, A. High-capacity room-temperature hydrogen storage of zeolitic imidazolate framework/graphene oxide promoted by platinum metal catalyst. *Int. J. Hydrogen Energy* **2015**, *40*, 12275–12285. [CrossRef]
11. Chen, Y.; Habibullah; Xia, G.; Jin, C.; Wang, Y.; Yan, Y.; Chen, Y.; Gong, X.; Lai, Y.; Wu, C. Palladium-Phosphide-Modified Three-Dimensional Phospho-Doped Graphene Materials for Hydrogen Storage. *Materials* **2023**, *16*, 4219. [CrossRef] [PubMed]
12. Lee, B.; Cho, S.; Jeong, B.J.; Lee, S.H.; Kim, D.; Kim, S.H.; Park, J.-H.; Yu, H.K.; Choi, J.-Y. Highly responsive hydrogen sensor based on Pd nanoparticle-decorated transfer-free 3D graphene. *Sens. Actuators B* **2024**, *401*, 134913. [CrossRef]
13. Liua, Y.; Zhang, Z.; Wang, T. Enhanced hydrogen storage performance of three-dimensional hierarchical porous graphene with nickel nanoparticles. *Int. J. Hydrogen Energy* **2018**, *43*, 11120–11131. [CrossRef]
14. Kula, P.; Szymanski, W.; Kolodziejczyk, L.; Atraszkiewicz, R.; Grabarczyk, J.; Clapa, M.; Kaczmarek, L.; Jedrzejczak, A.; Niedzielski, P. High strength metallurgical graphene for hydrogen storage nanocomposites. *Vacuum* **2016**, *129*, 79–85. [CrossRef]
15. Hussain, S.; Maktedar, S.S. Structural, functional and mechanical performance of advanced Graphene-based composite hydrogels. *Results Chem.* **2023**, *6*, 101029. [CrossRef]
16. Yuan, Y.; Rong, J.; Zheng, L.; Hu, Z.; Hu, S.; Wu, C.; Zhuang, Z. Control of the metal-support interactions in Ru on N-doped graphene-encapsulated Ni nanoparticles to promote their hydrogen evolution reaction catalytic performance. *Int. J. Hydrogen Energy* **2024**, *52*, 687–695. [CrossRef]
17. Rouquerol, J.; Avnir, D.; Fairbridge, C.W.; Everett, D.H.; Haynes, J.M.; Pernicone, N.; Ramsay, J.D.F.; Sing, K.S.W.; Unger, K.K. Recommendations for the characterization of porous solids. *Pure Appl. Chem.* **1994**, *66*, 1739–1758. [CrossRef]
18. Xu, L.; Hao, J.; Wang, J.; Yang, Y.; Zhao, R.; Zhang, R.; Yang, X. N doping porous carbon embedded in self-assembled three-dimensional reduced graphene oxide networks for electrochemical hydrogen storage. *Int. J. Hydrogen Energy* **2024**, *50*, 910–919. [CrossRef]
19. Han, D.C.; Zhang, C.M.; Guan, J.; Gai, L.H.; Yue, R.Y.; Liu, L.N.; Afzal, M.Z.; Song, C.; Wang, S.G.; Sun, X.F. High-performance capacitive deionization using nitrogen and phosphorus-doped three-dimensional graphene with tunable pore size. *Electrochim. Acta* **2020**, *336*, 135639. [CrossRef]
20. Wang, B.; Qin, Y.; Tan, W.; Tao, Y.; Kong, Y. Smartly designed 3D N-doped mesoporous graphene for high-performance supercapacitor electrodes. *Electrochim. Acta* **2017**, *241*, 1–9. [CrossRef]
21. Liu, H.; Wang, B.; Liu, H.; Zheng, Y.; Li, M.; Tang, K.; Pan, B.; Liu, C.; Luo, J.; Pang, X. Multi-crosslinked robust alginate/polyethyleneimine modified graphene aerogel for efficient organic dye removal. *Colloids Surf. A* **2024**, *683*, 133034. [CrossRef]
22. Bai, H.; Li, C.; Wang, X.; Shi, G. A pH-sensitive graphene oxide composite hydrogel. *Chem. Commun.* **2010**, *46*, 2376–2378. [CrossRef]
23. Kaczmarek, Ł.; Warga, T.; Makowicz, M.; Kyzioł, K.; Bucholc, B.; Majchrzycki, Ł. The Influence of the Size and Oxidation Degree of Graphene Flakes on the Process of Creating 3D Structures during Its Cross-Linking. *Materials* **2020**, *13*, 681. [CrossRef]
24. Lin, Y.; Xu, K.; Cao, X.; Zhang, Z.; Wu, J. Role of nanotube chirality on the mechanical characteristics of pillared graphene. *Mech. Mater.* **2021**, *162*, 104035. [CrossRef]
25. Amiri, H.; Mohandesi, J.A.; Marashi, P. Tensile properties of pillared graphene block. *Mater. Sci. Eng. B* **2020**, *257*, 11455. [CrossRef]
26. Kaczmarek, Ł.; Warga, T.; Kołodziejczyk, Ł.; Louda, P.; Borůvková, K.; Niedzielski, P.; Szymański, W.; Voleský, L.; Pawłowski, W.; Zawadzki, P. Creation of a 3D structure based on the High Strength Metallurgical Graphene®. *Surf. Rev. Lett.* **2019**, *26*, 1850206. [CrossRef]
27. Muzyka, R.; Drewniak, S.; Pustelny, T.; Chrubasik, M.; Gryglewicz, G. Characterization of graphite oxide and reduced graphene oxide obtained from different graphite precursors and oxidized by different methods using Raman spectroscopy. *Materials* **2018**, *11*, 1050. [CrossRef]
28. Ma, B.; Rodrigez, R.D.; Ruban, A.; Pavlov, S.; Sheremet, E. The correlation between electrical conductivity and second-order Raman modes of laser-reduced graphene oxide. *Phys. Chem. Chem. Phys.* **2019**, *21*, 10125–10134. [CrossRef]
29. Alkhouzaam, A.; Qiblawey, H.; Khraisheh, M.; Atieh, M.; Al-Ghouti, M. Synthesis of graphene oxides particle of high oxidation degree using a modified Hummers method. *Ceram. Int.* **2020**, *46*, 23997–24007. [CrossRef]

30. Aliyev, E.; Filiz, V.; Khan, M.M.; Lee, Y.J.; Abetz, C.; Abetz, V. Structural characterization of graphene oxide: Surface functional groups and fractionated oxidative debris. *Nanomaterials* **2019**, *9*, 1180. [CrossRef]
31. Sing, K.S.W.; Everett, D.H.; Haul, R.A.; Moscou, L.; Pierotti, R.A.; Rouquerol, J.; Siemieniewska, T. Reporting physisorption data for gas/solid system with special reference to the determination of surface area and porosity. *Pure Appl. Chem.* **1985**, *57*, 603–619. [CrossRef]
32. Claramunt, S.; Varea, A.; Lopez-Diaz, D.; Velazquez, M.; Cornet, A.; Cierera, A. The importance of interbands on the interpretation of the raman spectrum of graphene oxide. *J. Phys. Chem. C* **2015**, *119*, 10123–10129. [CrossRef]
33. Morales-Acosta, D.; Flores-Oyervides, J.D.; Rodriguez-Gonzalez, J.A.; Sanchez-Padilla, N.M.; Benavides, R.; Fernandez-Tavizon, S.; Mercado-Silva, J.A. Comparative methods for reduction and sulfonation of graphene oxide for fuel cell electrode applications. *Int. J. Hydrogen Energy* **2019**, *44*, 12356–12364. [CrossRef]
34. Gupta, A.; Chen, G.; Joshi, P.; Tadigadapa, S.; Eklund, P.C. Raman Scattering from High-Frequency Phonons in Supported n-Graphene Layer Films. *Nano Lett.* **2006**, *6*, 2667–2673. [CrossRef]
35. Ferrari, A.C. Raman spectroscopy of graphene and graphite: Disorder, electron–phonon coupling, doping and nonadiabatic effects. *Solid State Commun.* **2007**, *143*, 47–57. [CrossRef]
36. Yang, J.; Pruvost, S.; Livi, S.; Duchet-Rumeau, J. The Role of Fluorinated IL as an Interfacial Agent in P(VDF-CTFE)/Graphene Composite Films. *Nanomaterials* **2019**, *9*, 1181. [CrossRef]
37. Tiwari, A.; Panda, S.K. Stiffness enhancement of polymer nanocomposites via graphene nanoplatelet orientation. *Polym. Eng. Sci.* **2024**, *64*, 1482–1493. [CrossRef]
38. Kamedulski, P.; Skorupska, M.; Binkowski, P.; Arendarska, W.; Ilnicka, A.; Lukaszewicz, J.P. High surface area micro-mesoporous graphene for electrochemical applications. *Sci. Rep.* **2021**, *11*, 22054. [CrossRef]
39. Khodabakhshi, S.; Fulvio, P.F.; Walton, K.S.; Kiani, S.; Niu, Y.; Palmer, R.E.; Barron, A.R.; Andreoli, E. High surface area microporous carbon nanocubes from controlled processing of graphene oxide nanoribbons. *Carbon* **2024**, *221*, 118940. [CrossRef]